Closed-Loop Control of Inductive WPT System Through Variable Inductor

IEEE Open Journal of
Power Electronics

Received 29 July 2024; accepted 22 August 2024. Date of publication 26 August 2024;
date of current version 24 September 2024. The review of this article was arranged by Associate Editor Al-Thaddeus Avestruz.

Digital Object Identifier 10.1109/OJPEL.2024.3450202

Closed-Loop Control of Inductive WPT System Through Variable Inductor

FABIO CORTI [1] (Member, IEEE), FRANCISCO JAVIER LOPEZ-ALCOLEA [2] (Member, IEEE), LUIGI SOLIMENE [3] (Member, IEEE), ALBERTO REATTI [1] (Member, IEEE), SALVATORE MUSUMECI [3] (Member, IEEE), PEDRO RONCERO-SANCHEZ [2] (Member, IEEE), AND ALICIA TRIVIÑO CABRERA [4] (Member, IEEE)

[1]Università di Firenze, 50139 Firenze, Italy
[2]School of Industrial Engineering, University of Castilla-La Mancha, 13005 Ciudad Real, Spain
[3]Politecnico di Torino, 10129 Torino, Italy
[4]Universidad de Malaga, 13001 Malaga, Spain

CORRESPONDING AUTHOR: FABIO CORTI (e-mail: fabio.corti@unifi.it)

This work was supported by the Vice-Rectorate for Science Policy of the UCLM under its pre-doctoral mobility scholarship. This publication is part of the project TED2021-132233B-I00 funded by MCIN/AEI/10.13039/501100011033 and by the European Union "NextGenerationEU"/PRTR. This work was supported by the University of Castilla-La Mancha (UCLM) and the European Regional Development Fund (ERDF) under the pre-doctoral scholarship 2020-UNIVERS-9820.

ABSTRACT This paper introduces a novel control approach for an LCC-S Wireless Power Transfer (WPT) system. The system's output voltage regulation is achieved through a variable inductor, leveraging magnetic core saturation. A comprehensive design methodology for the variable inductor tailored to the desired control characteristics is presented. Addressing a significant gap in the current literature, the paper addresses the non-trivial challenge of developing a small signal model that correlates output voltage variations with changes in inductance. To fill this gap, the proposed approach pioneers a transfer function, providing an accurate description of this dynamic. Additionally, a closed-loop control system is proposed for prompt adjustment of the output voltage. The efficacy of this control system is demonstrated even in the face of rapid load variations or misalignment, ensuring reliable regulation. The robustness and effectiveness of the proposed approach are substantiated through extensive experimental measurements, validating the theoretical and simulation results.

INDEX TERMS Wireless power transfer, variable inductor, control.

I. INTRODUCTION

Inductive Wireless Power Transfer (IWPT) facilitates the transfer of electrical power without the need for direct physical connections. The proven benefits of this technology have led to its widespread adoption across various sectors, including mobility and consumer electronics.

The performances of these systems are significantly influenced by the chosen control strategy. Notably, these systems frequently encounter misalignments between the primary and secondary coils, changing the operating conditions of the system. Therefore, effective control strategies are essential to enable real-time control and disturbance rejection. Several control strategies have been proposed for Inductive Wireless Power Transfer (IWPT) [1]. Fig. 1 illustrates the classification of these approaches, revealing two main discernible families.

The first family employs control through power converter modulation techniques. Techniques within this family include Pulse Width Modulation (PWM), Pulse Frequency Modulation (PFM), Phase Shift Modulation (PSM), and Pulse Density Modulation (PDM). These approaches are widely adopted, having undergone extensive study and testing across various applications. Table 1 summarizes the key advantages and disadvantages of each technique. For a comprehensive understanding of the adoption of each technique, relevant references have been provided for each approach [2], [3], [4], [5], [6], [7], [8], [9], [10], [11], [12], [13], [14], [15], [17], [18], [19], [20], [21].

The second family of controllers performs the output voltage regulation by modifying the value of a component within the system. Given that WPT systems operate

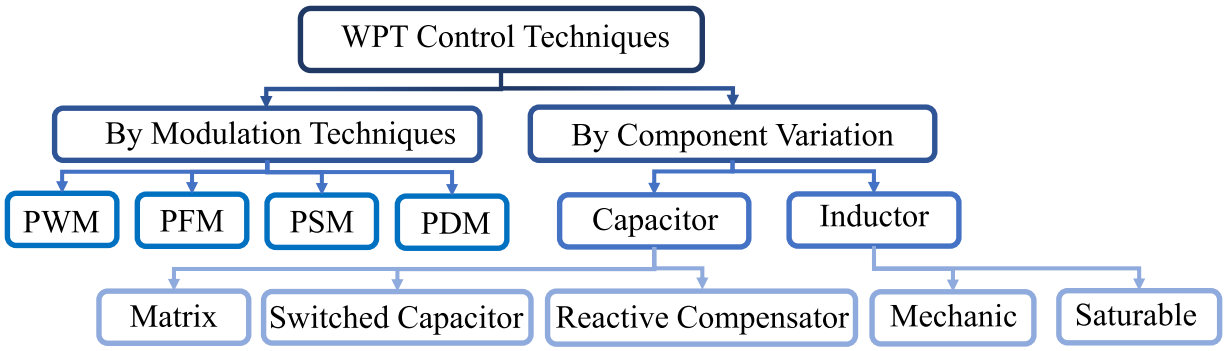

FIGURE 1. Classification of control techniques for WPT systems.

TABLE 1. Advantages and Disadvantages of Modulation Techniques

Modulation	Characteristics	Advantages	Disadvantages	Ref.
Pulse Width Modulation (PWM)	Fixed Frequency Variable Duty Cycle	• Operating at the resonant frequency enables maximum efficiency, regardless of the duty cycle. • Filtering circuits for fixed-frequency converters are easier to design than those for wide-frequency-range converters. • Operating at high frequency allows for low current/voltage ripple.	• Low efficiency at light load conditions due to switching losses.	[2], [3], [4], [5], [6], [7], [8], [9], [10]
Pulse Frequency Modulation (PFM)	Variable Frequency Fixed Duty Cycle	• At light loads, reducing the switching frequency decreases switching losses and consequently higher efficiencies are achieved.	• At low frequency, it increases the converter transient response time which could lead to slow response • Lower efficiency at heavy load.	[11], [12], [13], [14]
Pulse Density Modulation (PDM)	Fixed Frequency Fixed Duty Cycle Variable Number of Pulses	• Simpler control structure respect to PFM • Improved efficiency at low power loads	• High current/voltage ripple. • Switching frequency makes it easy to enter the audible noise range due to skipped cycles.	[17], [18], [19], [18]
Phase Shift Modulation (PSM)	Fixed Frequency Fixed Duty Cycle Variable Phase Shift	• Superior EMC performance. • Enhances efficiency by minimizing power semiconductor losses. Optimizing the phase shift enables more efficient inverter operation under specific load conditions.	• Achieving phase shift involves controlling the output of two power converters, introducing hardware complexity and increasing system costs.	[15], [16]

on the principles of resonance phenomena, these techniques involve adjusting the values of capacitances and/or inductances in the resonant compensation for regulation purposes. Table 2 provides an overview of the literature on controllers that involve varying components in WPT systems.

In the case of variable capacitance, the commonly employed method is the switched capacitor circuit. This circuit is created by connecting a power MOSFET in parallel with the resonant capacitor and controlling its conduction time using a PWM signal to modulate the equivalent capacitance seen by the circuit [22], [23], [24], [25], [26], [27]. This technique is particularly well-suited for Series-Series (SS) compensations due to its high sensitivity of the output voltage to variations of the resonant capacitance.

An alternative and noteworthy approach is introduced in [24], where the regulation is achieved through an active rectifier. Strategically switching an H-bridge, makes it possible to change the reactive power absorbed by the circuit, thus, simulating an effect equivalent to that of a variable capacitor.

Additionally, in [28] and [29], capacitance variation is achieved using a matrix of capacitors connected in series and/or parallel through power switches. However, this solution appears suboptimal, and the presence of numerous switches makes it unsuitable for high-power applications.

The main drawbacks of using switched capacitor circuits or matrix of capacitors in addition to the complex control are their complex control and their high power losses due to the use of multiple power switches operating on the resonant compensation.

Another resonant topology widely used is the LCC-S compensation. In this latter, differently from the SS compensation, the output voltage has low sensitivity to load variation, making it suitable for constant-voltage applications. As shown in the sensitivity analysis presented in [30], the output voltage is more sensitive to variations in inductance rather than capacitance. For this reason, works focused on the design of variable inductors have been carried out [31], [32], [33], [34], [35].

Concerning the implementation of variable inductance, [31] achieves variation by altering reluctance through a

TABLE 2. Literature Overview of WPT Controller by Component Variation

Ref.	Topology	Technique	N. Switches	N. Capacitors	N. Inductors	Auxiliary Circuit
[22]	SS	Switched Capacitor	2	4	0	-
[23]	Class-E	Switched Capacitor	1	2	0	-
[24]	SS	Switched Capacitor	4	1	0	-
[25]	SS	Switched Capacitor	2	4	0	-
[26]	LCC-S	Switched Capacitor	4	4	0	-
[27]	SS	Switched Capacitor	4	4	0	-
[28]	SS	Reactive Power Compensator	4	1	0	-
[29]	SS	Matrix Capacitor	6	12	0	-
[30]	SS	Matrix Capacitor	14	14	0	-
[32]	S-SP	Mechanical	0	0	1	Core Positioning System
[33]	Class-E	Passive Variable Inductor	0	0	2	Current Controller Converter
[34]	LCC-S	Passive Variable Inductor	2	1	1	Current Controller Converter
[35]	SS	Passive Variable Inductor	0	0	2	Current Controller Converter
[36]	SS	Passive Variable Inductor	0	0	1	Current Controller Converter

TABLE 3. Literature Overview of Converters Regulated With Passive Variable Inductor

Ref.	Topology	Analytical Steady-State Analysis	Experimental Validation	Dynamic Control
[39]	LLC Converter	YES	NO	NO
[40]	LLC Converter	YES	NO	NO
[41]	Buck Converter	YES	YES	NO
[42]	Buck Converter	NO	YES	YES
[43]	Three Phase Inverter	YES	YES	NO
[44]	Buck Converter for LED Lighting	YES	YES	NO
[45]	Dual Active Bridge	YES	YES	NO
[46]	LCC-S IWPT	YES	YES	NO

mechanical movement of the magnetic core relative to the coil. This solution is well-suited for high-precision positioning applications where inductance values must be adjusted based on the position.

The prevalent technique for WPT control through variable inductance involves exploiting core saturation to induce inductance variation [32], [33], [34], [35], [36], [37]. This effect is achieved by adjusting the current in an auxiliary winding connected to the core, thereby altering the operating point on the magnetic device B-H curve and, consequently, the differential permeability. This technique has been widely employed, not only in WPT applications but also in various other contexts, as illustrated in Table 3.

As shown in the table, all the papers currently available in the literature are focused on system design and steady-state analysis [38], [39], [40], [42], [43], [44], [45], [46]. This is because it is particularly difficult to model the dynamic effect that the inductance values variation produce on the system. In addition, no information is presented about the current regulation system in the active inductor, an aspect of primary importance that plays a key role in obtaining good dynamic performance. Therefore, the literature currently lacks a theoretical study that models the dynamic behavior of this system. For this reason, the main innovative aspects of this article are:

- To propose the analysis and design procedure of an auxiliary circuit for the DC current regulation of the variable inductor.
- To propose a small signal model that describes the effect that the variation in inductance produces on the WPT system output voltage of an LCC-S compensated system.
- To propose a closed-loop control system that allows the DC current of the variable inductor to be automatically adjusted to follow a specific output voltage profile.

The paper is organized as follows. In Section II, the LCC-S compensation and the principle of operation of the proposed control strategy are presented. In Section III, the design of the active inductor is shown. In Section III, the small-signal model of the system is derived. In Section IV, the control loop is presented. In Section V, the theoretical measurements are validated experimentally. Finally, in Section VI, the conclccusions are derived.

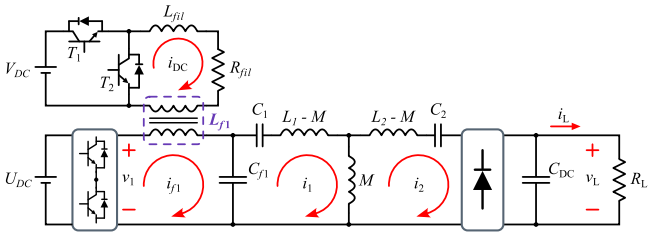

FIGURE 2. Proposed scheme of the LCC-S compensated magnetic coupler with passive variable inductor.

II. LCC-S COMPENSATION MODELING

This section aims to explain the operation of the proposed IWPT system, depicted in Fig. 2. The IWPT is composed of a half-bridge inverter, the LCC-S compensated magnetic coupler, and a rectifier with a resistive load. The filter inductance of the LCC compensation is connected to an auxiliary DC-DC converter that allows modification of its inductance as explained in Section III.

The phasor of the first-harmonic of the square voltage impressed by the inverter is [47]:

$$\hat{V}_1 = |V_1|e^{j0^\circ} = \frac{2}{\pi}U_{DC} \tag{1}$$

where U_{DC} is the DC input voltage as shown in Fig. 2. The T-equivalent model is used for the coupled coils. When the LCC-S compensated IWPT system operates at a resonant frequency f_0, the phasor of the current at the output of the half-bridge inverter is:

$$\hat{I}_{f1} = \frac{Z_1 Z_2 + \omega^2 M^2}{Z_{f1}(Z_1 Z_2) + \omega^2 M^2 - Z_{Cf1}^2 Z_2}\hat{V}_1 \tag{2}$$

where $M = k\sqrt{L_1 L_2}$ is the mutual inductance and k is the coupling coefficient. The phasor of the secondary side current is:

$$\hat{I}_2 = \frac{j\omega M Z_{Cf1}}{Z_{f1}(Z_1 Z_2 + \omega^2 M^2) - Z_{Cf1}^2 Z_2}\hat{V}_1 \tag{3}$$

where:

$$\begin{aligned} Z_{f1} &= j\omega L_{f1} + \frac{1}{j\omega C_{f1}} \\ Z_{Cf1} &= \frac{1}{j\omega C_{f1}} \\ Z_1 &= j\omega L_1 + \frac{1}{j\omega C_1} + \frac{1}{j\omega C_{f1}} \\ Z_2 &= j\omega L_2 + \frac{1}{j\omega C_2} + \frac{8}{\pi^2}R_L \end{aligned} \tag{4}$$

The DC value of the output current after the rectifier applied to the resistive load R_L can be expressed as a function of $\hat{I}_2$ as follows [48]:

$$I_L = \frac{2}{\pi}|\hat{I}_2| \tag{5}$$

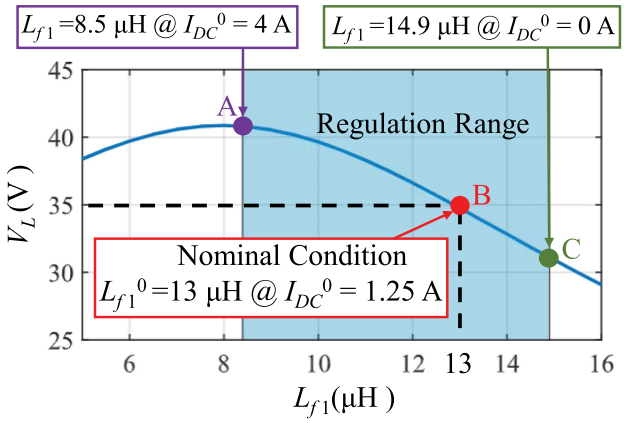

FIGURE 3. Variation of output voltage V_L versus changes in L_{f1} in the proposed system. The red point represents the nominal operating condition.

TABLE 4. Characteristics of the Proposed LCC-S System

Parameter	Value	Parameter	Value
U_{DC} (V)	28	L_{f1}^0 (µH)	13
C_{f1} (nF)	353	C_1 (nF)	43.8
L_1 (µH)	85.5	L_2 (µH)	92.9
C_2 (nF)	33.2	C_{DC} (µF)	390
R_L (Ω)	50	k	0.34
f_0 (kHz)	85	M (µH)	30.3

TABLE 5. System Parameters: Buck Converter

Parameter	Value	Parameter	Value
V_{DC} (V)	5	L_{fil} (mH)	1
R_{fil} (Ω)	1	I_{DC}^0 (A)	1.25

Therefore, the load voltage can be expressed as:

$$V_L = \frac{2}{\pi}|\hat{I}_2|R_L \tag{6}$$

Fig. 3 shows V_L as a function of L_{f1} for an IWPT system with the parameter values collected in Table 4 and Table 5. In this figure, it is shown that V_L has a direct linear relationship between both variables for a certain range. The minimum V_L that can be reached for a given coupling coefficient k depends on the maximum inductance that can be achieved with L_{f1}. Moreover, it is found that, over certain L_{f1} value, when L_{f1} reduces, V_L does not increase, even changing the tendency to a decrease of this voltage.

The shadowed area in Fig. 3 shows the operating range of the proposed IWPT system, delimited by the minimum and maximum values of L_{f1} that will be used. From this graph, it is predicted that a 20% V_L regulation is achieved. The red dot marks the load voltage at the equilibrium point defined in Section IV that will be used for the tuning of the controllers in Section V.

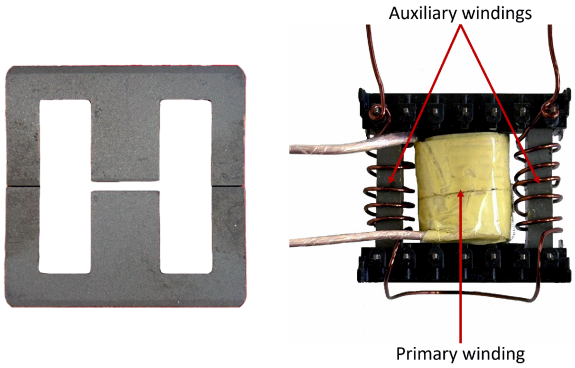

FIGURE 4. Picture of the realized variable inductor, with a detail of the central gapped double-E core and the arrangement of the windings.

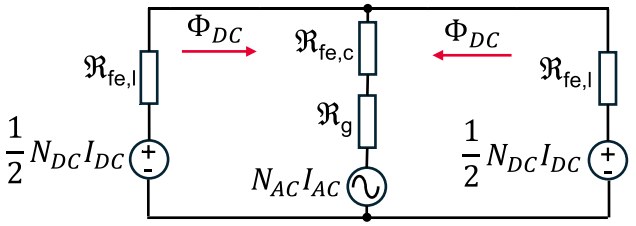

FIGURE 5. Lumped equivalent reluctance circuit of the double-E core. The magnetomotive force sources associated with the AC and DC windings are reported.

III. PASSIVE VARIABLE INDUCTOR: PRINCIPLE OF OPERATION AND DESIGN

The input inductor of the LCC-S compensation scheme can be implemented as a variable inductor to tune the inductance value to regulate the transmitted power of the IWPT system. A variable inductor can be implemented in several ways. A basic approach is adopting a reconfigurable inductance network, realized through several discrete fixed-value inductors connected in series or parallel. A further approach is the adoption of a mechanically controlled variable inductor, where the inductance value is regulated by adjusting the air gap of the magnetic core. The solution adopted in this paper is a variable inductor realized by controlling the operating point of a magnetic core through an auxiliary winding fed by a DC current. The most straightforward structure is thus made of two windings: a primary winding connected to the compensation network and an auxiliary winding for the inductance regulation.

A double-E core structure is a more reliable magnetic structure for implementing a variable inductor because the primary winding can be located on the central column of the core, while the auxiliary winding can be split on the outer legs of the core with an anti-series connection, as shown in Fig. 4. This configuration has the main advantage of controlling the magnetization of the outer path of the core, while it does not considerably influence the magnetic operation of the central column. In addition, an air gap can be realized on the central column to prevent the core saturation. With the magnetization control of the sole outer path and the addition of an air gap on the central column, a smoother inductance variation can be obtained, making the magnetization control more reliable. Another advantage of the double-E structure with the anti-series connection is the canceling of the electromotive forces induced on the auxiliary circuit, and this helps in the regulation of the magnetizing current. The control of the magnetizing current for the auxiliary winding can be suitably implemented through a DC-DC buck converter, as illustrated in Fig. 2. An analytical approach can be followed to design a double-E core-based variable inductor by adopting the lumped equivalent reluctance model depicted in Fig. 5.

The inductance referred to the AC winding L depends on its number of turns N_{AC} and the equivalent reluctance $\mathcal{R}_{\text{eq}}$. Regulating the current I_{DC} on an additional winding with N_{DC} turns can change the magnetic operating point of the core material and thus the equivalent reluctance referred to the AC winding. Therefore, the reluctance is a function of the number of turns N_{DC} and the current I_{DC} ($\mathcal{R}_{\text{eq}}(N_{\text{DC}}I_{\text{DC}})$) [45]. The equivalent inductance can be expressed as:

$$L = \frac{N_{\text{AC}}^2}{\mathcal{R}_{\text{eq}}(N_{\text{DC}}I_{\text{DC}})}, \tag{7}$$

where $\mathcal{R}_{\text{eq}}$ is the equivalent reluctance referred to the AC winding. Its value can be determined on the lumped equivalent reluctance model by replacing the DC magnetomotive force sources with a short circuit and evaluating the equivalent reluctance view at the terminals of the AC magnetomotive force source, which can be expressed as

$$\mathcal{R}_{\text{eq}}(N_{\text{DC}}I_{\text{DC}}) = \mathcal{R}_{\text{tot,c}} + 0.5\,\mathcal{R}_{\text{fe,l}}(N_{\text{DC}}I_{\text{DC}}). \tag{8}$$

The reluctance of the central column $\mathcal{R}_{\text{tot,c}}$ is defined as the series of the magnetic material path reluctance (fe) and the air gap reluctance (g):

$$\mathcal{R}_{\text{tot,c}} = \mathcal{R}_{\text{fe,c}} + \mathcal{R}_{\text{g}} = \frac{l_{\text{fe,c}}}{\mu_0\,\mu_{\text{fe}}\,S_{\text{fe,c}}} + \frac{l_{\text{g}}}{\mu_0\,S_{\text{g}}}, \tag{9}$$

where $l_{fe,c}$ represents the magnetic path length of the central core columns, l_g is the air gap length, $S_{fe,c}$ is the cross-section of the central column, and S_g is the cross-section of the air gap, assumed to be equal to the core cross-section. μ_{fe} is the relative permeability of the magnetic material and μ_0 is the vacuum permeability. The reluctance of the central column is assumed to be constant since it is not influenced by the magnetic field caused by the DC magnetizing current. The reluctance of the outer column $\mathcal{R}_{\text{fe,l}}$ is

$$\mathcal{R}_{\text{fe,l}}(N_{\text{DC}}I_{\text{DC}}) = \frac{l_{\text{fe,l}}}{\mu_0\,\mu_{\text{fe}}(N_{\text{DC}}I_{\text{DC}})\,S_{\text{fe,l}}}. \tag{10}$$

where the relative permeability of the magnetic material $\mu_{fe}(N_{DC}I_{DC})$ is a function of the magnetizing current, which controls the magnetic field in the outer path of the core. The selection of the geometrical specifications of the core, the air gap, the number of turns of the primary, and the

TABLE 6. Specifications of the Realized Variable Inductor

Parameter	Value
Core material	N87 ferrite
Core geometry	E 32/16/9
Air gap length	1 mm
AC winding turns N	10
DC winding turns N_{DC}	10 $(5+5)$
Nominal inductance @ $I_{\mathrm{DC}}=0$ A	14.9 μH
Saturated inductance @ $I_{\mathrm{DC}}=4$ A	8.3 μH

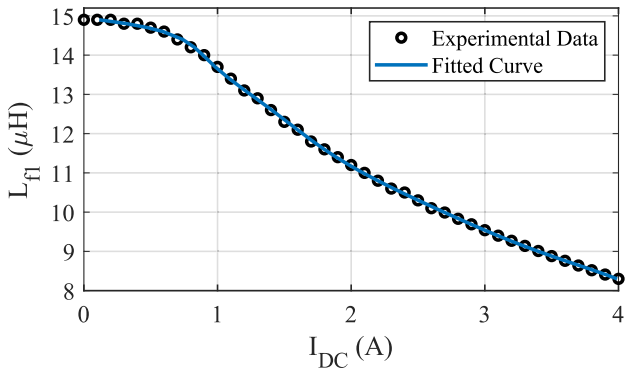

FIGURE 6. Inductance profile as a function of the magnetizing current: Experimental data vs curve fitting.

magnetizing winding allows for realizing the required inductance variation for regulating the IWPT system. For the realized experimental setup, an initial inductance of 13 μH is required, with a saturated value of 8 μH, to reach the peak of the load voltage, and thus the peak of the transmitted output power. To this end, the design specifications presented in Table 6 are selected.

The obtained inductance profile as a function of the magnetizing current is represented in Fig. 6. The curve fitting shown in this Figure will be explained later in Section V.

The core material selection is a critical choice, since a smooth differential permeability profile is required to obtain a smooth inductance decrease as a function of the magnetizing current. To this aim, metal powder materials can represent a good solution with their distributed air gap property [49]. However, the input inductor of the LCC-S compensation scheme is also affected by high-frequency voltage waveforms, which severely impact the magnetic losses of the core. In this sense, the bad specific loss properties of metal powder cores do not represent the best choice. On the other hand, the adoption of a ferrite core (N87, TDK) represents a good trade-off between competitive specific loss properties at high frequency and the obtained inductance profile. The permeability drop of the N87 ferrite is quite sharp compared to a metal powder material, but the addition of an air gap and the selected double-E core configuration help reach a suitable profile for the regulation of the IWPT system.

A. ANALYSIS OF THE INDUCTOR POWER LOSSES

The adoption of a controlled variable inductor for regulating IWPT systems requires evaluating the power loss introduced by the device. A conventional single-winding inductor, needed for an LCC-S compensation network, incurs magnetic core losses and winding ohmic losses. On the other hand, a double-E core variable inductor also brings in ohmic losses related to the auxiliary magnetizing current, along with increased core losses due to core saturation. The ohmic losses of the AC winding are determined using the root mean square (RMS) value of the AC current and the high-frequency resistance of the AC winding. To reduce the high-frequency resistance, the AC winding has been constructed using litz wire. The resistance measured at a frequency of 85 kHz is reported as $R_{\mathrm{AC}} = 24.1$ mΩ [45]. The DC winding losses can be calculated by using the current value of the DC auxiliary winding and the resistance of the winding, whose measured value is $R_{\mathrm{DC}} = 74.3$ mΩ. If the cancellation of the electromotive forces induced on the auxiliary circuit is incomplete, a high-frequency current flows in the DC winding, introducing an additional power loss term. This value is critical to estimate through analytical computations or simulations. However, considering the reduced RMS value of the high-frequency current in the auxiliary winding compared to the main currents in the AC and the DC windings, this loss term can be considered negligible without excessively affecting the power loss estimation. As previously mentioned, the magnetic core losses are influenced by the effect of the magnetization determined by the auxiliary winding, which brings the core's outer legs to operate in saturated conditions. For soft ferrite materials, particularly for the N87 ferrite, the literature indicates an increase in the magnetic core losses when the DC magnetic bias increases [50]. Calculating the magnetic core losses for the variable inductor is challenging due to the varying magnetic flux density conditions in different sections of the core. The outer path of the core is only affected by the DC magnetic field bias when the magnetization winding is supplied. An estimation of the magnetic core losses under DC bias can be performed through the MagNet AI, a data-driven method to describe core losses under different operating conditions, including different DC bias values [51], [52]. We used the MagNet AI to compute the volumetric core losses for the N87 material under the operating conditions of the considered application. In particular, for the central column losses $P_{\mathrm{C,cen}}$, we considered the operating flux density waveform at 85 kHz without DC bias, while for the outer path losses $P_{\mathrm{C,out}}$, we also considered the DC bias value corresponding to the operation of the controlled variable inductor in the saturated state. Table 7 reports the estimation of the inductor losses when operating with a DC magnetizing current of 3A.

From these results, it is apparent how the main loss contributions are related to the inductor operation with a DC magnetizing current since the terms associated with the DC winding losses and the core losses of the outer path are the

TABLE 7. Estimated Power Losses of the Controlled Variable Inductor, $I_{DC} = 3$ A

Power Loss	Value	Loss term	Value
$P_{W,AC}$ (W)	0.488	$P_{W,DC}$ (W)	0.669
$P_{C,cen}$ (W)	0.088	$P_{C,out}$ (W)	0.659
P_{TOT} (W)		1.904	

more significant. The operation of the inductor in the unsaturated state will result in reduced power losses. Also, the WPT system achieves its maximum power transfer condition during saturated operation, as illustrated in Fig. 3. The additional energy required to reach the saturated condition aligns with the maximum output power delivery, thus contributing to maintaining high overall IWPT system efficiency.

IV. SMALL-SIGNAL MODEL DERIVATION

This section aims to develop the small-signal model of the system, obtaining the transfer functions that will be used for implementing the proposed control scheme. For this purpose, the IWPT system, the rectifier, and the DC-DC converter are examined.

A. INDUCTIVE WIRELESS POWER TRANSFER SYSTEM MODEL

The three Kirchhoff Voltage Laws that describe the circuit shown in Fig. 2 are:

$$v_{in}(t) = R_{Lf1} i_{f1}(t) + L_{f1}(t)\frac{di_{f1}(t)}{dt} + i_{f1}(t)\frac{dL_{f1}(t)}{dt} + \frac{1}{C_{f1}}\int [i_{f1}(t) - i_1(t)]dt + R_{Cf1}[i_{f1}(t) - i_1(t)], \tag{11}$$

$$\frac{1}{C_{f1}}\int [i_{f1}(t) - i_1(t)]dt + R_{Cf1}[i_{f1}(t) - i_1(t)] = \frac{1}{C_1}\int i_1(t)dt + R_1 i_1(t) + (L_1 - M)\frac{di_1(t)}{dt} + M\frac{d[i_1(t) - i_2(t)]}{dt}, \tag{12}$$

$$M\frac{d[i_1(t) - i_2(t)]}{dt} = (L_2 - M)\frac{di_2(t)}{dt} + R_2 i_2(t) + \frac{1}{C_2}\int i_2(t)dt + R_L i_2(t). \tag{13}$$

In (11), there are two non-linear terms, that multiply the variables $L_{f1}(t)$ and $i_{f1}(t)$. After linearizing around the equilibrium point defined by equations (1) to (6), the Laplace transform is used, obtaining the following expressions in the continuous-time domain:

$$\begin{aligned} \Delta V_{in}(s) &= Z_{f1}(s)\Delta I_{f1}(s) + sI^0_{f1}\Delta L_{f1}(s) - Z_{Cf1}(s)\Delta I_1(s) \\ Z_{Cf1}(s)\Delta I_{f1}(s) &= Z_1(s)\Delta I_1(s) - sM\Delta I_2(s) \\ sM\Delta I_1(s) &= Z_2(s)\Delta I_2(s) \end{aligned} \tag{14}$$

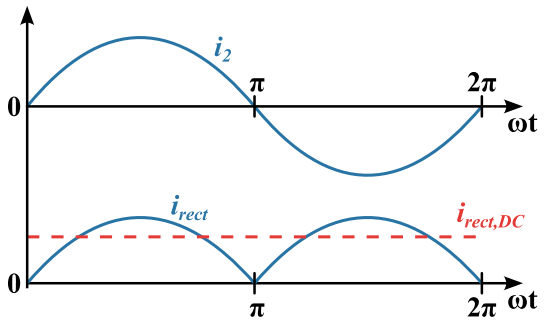

FIGURE 7. Currents at the AC and DC sides of the rectifier.

where:

$$\begin{aligned} Z_{Lf1}(s) &= R_{Lf1} + R_{Cf1} + sL^0_{Lf1} + \frac{1}{sC_{f1}} \\ Z_{Cf1}(s) &= R_{Cf1} + \frac{1}{sC_{f1}} \\ Z_1(s) &= R_{Cf1} + R_1 + sL_1 + \frac{1}{sC_1} + \frac{1}{sC_{f1}} \\ Z_2(s) &= R_2 + R_L + sL_2 + \frac{1}{sC_2} \end{aligned} \tag{15}$$

From (14), the transfer function that relates the increments in the inductance, ΔL_{f1}, and the current, ΔI_2, is:

$$H_{IPT}(s) = \frac{\Delta I_2(s)}{\Delta L_{f1}(s)} = -\frac{s^2 M I^0_{f1} Z_{Cf1}}{Z_{f1}[Z_1 Z_2 - s^2 M^2] - Z^2_{Cf1} Z_2} \tag{16}$$

B. RECTIFIER

Equation (16), shows that the LCC-S compensated magnetic coupler has a current-source behavior. Consequently, by applying the first-harmonic approximation, the currents in the AC and DC side of the rectifier (I_2 and I_{rect}, respectively) are those shown in Fig. 7.

The current I_{rect} can be expressed as a Fourier series as:

$$i_{rect}(\omega t) = \frac{a_0}{2} + \sum_{n=1}^{\inf}[a_n \cos(n\omega t) + b_n \sin(n\omega t)] \tag{17}$$

Therefore, the DC value of I_{rect}, $I_{rect,DC}$, are calculated as:

$$I_{rect,DC} = \frac{a_0}{2} = \frac{1}{\pi}\int_0^{\pi} i_2(\omega t)d\omega t \tag{18}$$

By using the first harmonic approximation one gets

$$i_2(\omega t) = \hat{I}_2 \sin(\omega t) \tag{19}$$

and, by using equations (18) and (19), the following relationship is obtained:

$$I_{rect,DC} = \frac{2}{\pi}\hat{I}_2 \tag{20}$$

which can be written in the small-signal model as:

$$\Delta I_{rect,DC}(s) = \frac{2}{\pi}\Delta I_2(s) \tag{21}$$

The DC load connected to the rectifier consist of an RC circuit with time constant $\tau_{DC} = 1/(RC_{DC})$. The relationship between I_{rect} and the output voltage V_L in the continuous time domain is:

$$V_L(s) = \frac{R_L}{sC_{DC}R_L + 1} I_{rect}(s) \tag{22}$$

Therefore, the relationship between $\Delta V_L(s)$ and $\Delta I_2(s)$ is:

$$\Delta V_L(s) = \frac{2}{\pi}\frac{R_L}{sC_{DC}R_L + 1}\Delta I_2(s) \tag{23}$$

The dynamic of the transfer function shown in (16) is characterized by a pair of complex conjugate poles that fulfill the following equation:

$$s^2 + a_1 s + a_0 = s^2 + 2\zeta\omega_n s + \omega_n^2 \tag{24}$$

where $\omega_n = \sqrt{a_0}$ is the natural frequency of the poles and $\zeta = a_1/(2\sqrt{a_0})$ is the damping coefficient. The time constant for the two conjugate complex poles is:

$$\tau_{IPT} = \frac{1}{\zeta\omega_n} \tag{25}$$

Provided that $\tau_{RC} >> \tau_{IPT}$, the evolution of V_L will be determined by the RC circuit. This holds true for the IPT system used in this article, where $\tau_{RC} = 19.5$ ms and $\tau_{IPT} = 128\,\mu$s. Therefore, the transfer function (16) can be simplified by approximating it to a first-order system:

$$\Delta I_2(s) \approx -|H_{IPT}(j\omega_0)|\frac{1}{\tau_{IPT}s + 1}\Delta L_{f1}(s) \tag{26}$$

where ω_0 is the operating frequency of the IWPT system.

Finally, by using equations (23) and (26), the transfer function $H_V = \Delta V_L(s)/\Delta L_{f1}(s)$ is obtained:

$$H_V(s) = -\frac{2}{\pi}|H_{IPT}(j\omega_0)|\frac{1}{\tau_{IPT}s + 1}\cdot\frac{R_L}{sC_{DC}R_L + 1} \tag{27}$$

C. DC-DC CONVERTER

The equation that defines the behavior of the DC-DC converter when T1 is switched ON and T2 is OFF is:

$$v_{DC} = L_{fil}\frac{di_{DC}(t)}{dt} + R_{fil}i_{DC}(t) + L_{f1}(t)\frac{di_{DC}(t)}{dt} + i_{DC}(t)\frac{dL_{f1}(t)}{dt} \tag{28}$$

whereas when T1 is OFF and T2 is switched ON, the following expression explains the behavior of the DC-DC converter:

$$0 = L_{fil}\frac{di_{DC}(t)}{dt} + R_{fil}i_{DC}(t) + L_{f1}(t)\frac{i_{DC}(t)}{dt} + i_{DC}(t)\frac{L_{f1}(t)}{dt} \tag{29}$$

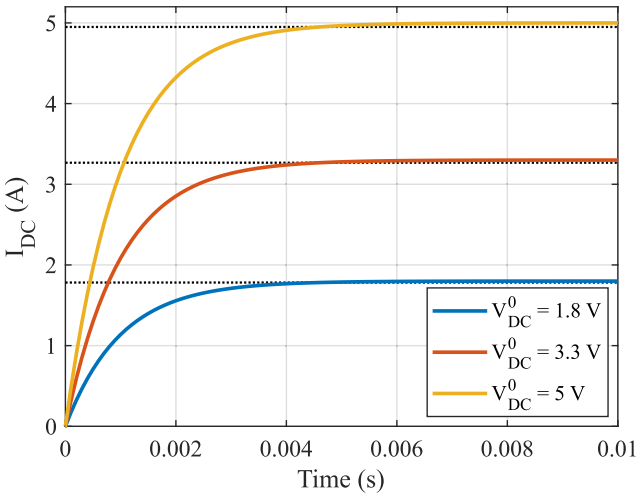

FIGURE 8. Evolution of I_{DC} when D changes from 0 to 1 for different values of V_{DC}^0.

Equations (28) and (29) have non-linear terms. Therefore, the system must be linearized around the equilibrium point defined by the following equation:

$$I_{DC}^0 = \frac{V_{DC}^0 D^0}{R_{fil}} \tag{30}$$

where D^0 is the duty cycle applied to the DC-DC converter in the equilibrium point.

The linearization of equations (28) and (29) yields:

$$\Delta v_{DC}(t)\Delta d(t) = L_{fil}\frac{\Delta i_{DC}(t)}{dt} + R_{fil}\Delta i_{DC}(t) + \Delta L_{f1}(t)\frac{\Delta i_{DC}(t)}{dt} + \Delta i_{DC}(t)\frac{\Delta L_{f1}(t)}{dt} \tag{31}$$

and after applying the Laplace transform, the following expression in the continuous-time domain is obtained:

$$V_{DC}^0\Delta D(s) + D^0\Delta V_{DC}(s) = sL_{fil}\Delta i_{DC}(s) + R_{fil}\Delta I_{DC}(s) + sL_{f1}^0\Delta I_{DC}(s) + sI_{DC}^0\Delta L_{f1}(s) \tag{32}$$

Consequently, by taking $\Delta V_{DC}(s)$ and $\Delta L_{f1}(s)$ as disturbances in the system, the transfer function $H_I(s) = \Delta I_{DC}(s)/D(s)$ is:

$$H_I(s) = \frac{V_{DC}^0}{s(L_{fil} + L_{f1}^0) + R_{fil}} \tag{33}$$

The transfer function $H_I(s)$ has a time constant $\tau_{DC} = (L_{fil} + L_{f1}^0)/R_{fil}$. When the inductance L_{fil} significantly exceeds that of the variable inductor, this time constant can be approximated as $\tau_{DC} \approx L_{fil}/R_{fil}$. For a first order system, the 1% settling time will be approximately 4.6 times τ_{DC}, as illustrated in Fig. 8. In this Figure, the evolution of i_{DC} in response to a step change in D from 0 to 1 is shown for three different values of V_{DC}^0. The dotted lines represent 99% of the corresponding final value of i_{DC}. While the maximum value obtained for i_{DC} varies with V_{DC}^0, the settling time remains

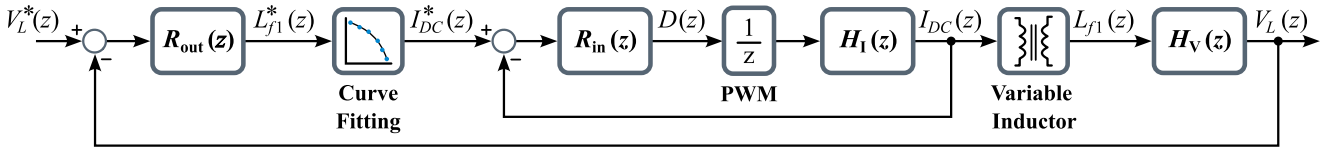

FIGURE 9. Proposed Control Scheme.

TABLE 8. Fitting Coefficients

Coef.	Value	Coef.	Value
c_0	-38679.2037	c_5	13.4424
c_1	28450.2720	c_6	-0.6008
c_2	-9101.8901	c_7	0.0152
c_3	1654.5880	c_8	$-1.6867 \cdot 10^{-4}$
c_4	-186.9399		

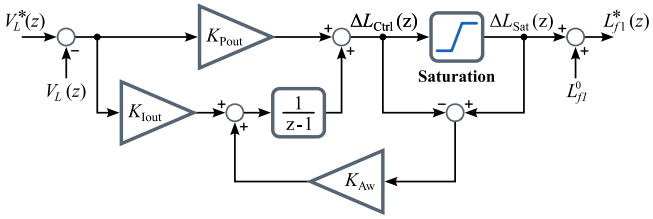

FIGURE 10. Proposed control scheme for the outer Loop.

constant across all cases. This scenario represents the most significant variation in D achievable in the DC-DC converter, resulting in the fastest settling time that can be obtained without modifying L_{fil} or R_{fil}.

The control loop will be implemented in the discrete time domain. Therefore, the discretization of both $H_I(s)$ and $H_V(s)$ was performed. For this purpose, the zero order hold discretization method was selected, with a sampling period $T_s = 1/f_s$. The obtained transfer functions are shown below:

$$H_V(z) = \frac{b_1 z + b_0}{z^2 + a_1 z + a_0} \tag{34}$$

$$H_I(z) = \frac{b_2}{z - a_2} \tag{35}$$

V. CONTROL LOOP DESIGN

The proposed control scheme is shown in Fig. 9. It is composed of two nested control loops designed in the discrete-time domain with a sampling frequency $f_s = 10$ kHz. The outer one regulates the voltage delivered to the load and indicates the value of L_{f1} that must be achieved for following the reference voltage V_L^*. A polynomial expression translates this desired inductance into the DC current that the DC-DC converter must provide to the inductor. Finally, the inner control loop compares this current with the measured one and changes the duty cycle of the DC-DC converter according to it. In the inner controller, a delay of one sample is added because of the PWM generation and the calculation of the control signals.

To ensure the proper behavior of the control scheme, the dynamics of the inner loop must be faster than that of the outer loop. This reduces the interaction between the dynamics of the two controllers and allows an easier tuning of both controllers.

Another aspect that must be taken into account is the dynamic of the changes in the inductance of L_{f1}. The current at the output of the DC-DC converter modifies the inductance values, and measuring this dynamic is not straightforward. However, if the changes are fast enough, it can be assumed to be instantaneous in practice. Therefore, the combination of the inner control loop, the curve fitting and the inductor dynamics can be regarded as transparent during the design of the outer controller.

A. OUTER CONTROL LOOP

The proposed scheme for the outer loop is shown in Fig. 10. It is composed of a proportional-integral (PI) regulator $R_{out}(z)$, and an anti-windup action.

The proportional and integral gains of the $R_{out}(z)$ (K_{Pout} and K_{Iout}, respectively) modify the desired value of L_{f1} according to the tracking error of the reference voltage. The inductance of the passive variable inductor can vary within the range $[L_{min}, L_{max}]$. Therefore, the control signal must not be outside these limits to avoid instability issues.

For this purpose, the saturation is placed at the output of the control signal. This ensures that the desired value of L_{f1} can be achieved. During the initialization of the controller or when compensating for a disturbance, the control signal can exceed these limits. Then, the integral part of the control signal can start increasing significantly. As a result, the control output remains in the saturation state for long periods of time, even when the tracking error is small.

To avoid this effect, an anti-windup action is implemented. It modifies the value of the integral part of the regulator only when its output signal, $\Delta L_{Ctrl}(z)$, is different from the applied one, ΔL_{Sat}. Its behavior is modulated through the gain K_{Aw}. The greater its value is, the more it will modify the output of the integral part of the regulator.

B. CONVERSION OF L_{f1} TO I_{DC}^*

The translation of the control signal into the reference current for the inner loop is achieved by using the experimental data shown in Fig. 6. It relates the measured value of L_{f1} with the applied current I_{DC}. It is obtained that the relationship between L_{f1} and I_{DC} is not linear. Consequently, the evolution of the data has been fitted by using the *polyfit* function of

TABLE 9. Control Specifications

Spec.	Inner Loop	Outer Loop
Rise Time (ms)	5	50
Settling Time (ms)	15	150

TABLE 10. Control Parameters

Parameter	Value	Parameter	Value
K_{Pout}	$-2 \cdot 10^{-7}$	K_{Pin}	0.035
K_{Iout}	$-1.35 \cdot 10^{-9}$	K_{Iin}	0.007
KAw	0.001		

MATLAB with an eight order polynomial:

$$I_{DC}^{*} = \sum_{n=0}^{8} c_n (L_{f1})^n \tag{36}$$

where the obtained coefficients are summarized in Table 8.

The predicted trend is compared to the experimental data in Fig. 6. It results in a good fitting that allows to *translate* the target inductance L_{f1} provided by the outer control loop into the reference current I_{DC} for the inner controller.

A lookup table is also suitable for this purpose. The measured values in Fig. 6 can be stored, using interpolation to obtain the target inductance L_{f1}. However, polynomial fit has lower memory usage, as only the nine coefficients of the polynomial need to be stored, rather than all the measured data.

C. INNER CONTROL LOOP

The inner control loop integrates a conventional PI regulator $R_{in}(z)$ with proportional and integral gains K_{Pin}, K_{Iin}:

$$R_{in}(z) = K_{Pin} + \frac{K_{Iin}}{z-1} \tag{37}$$

It evaluates the tracking error of the reference current and modifies the duty cycle applied to the DC-DC converter according to it.

D. TUNING

The tunings of the inner and outer loops are made separately. As stated before, the settling times of both controllers must be different, being the dynamic response of the inner loop faster than that of the outer controller. The tuning of both $R_{out}(z)$ and $R_{in}(z)$ is made by using the transfer functions $H_V(z)$ and $H_I(z)$, respectively. For each regulator, the maximum 0 to 80% rise and 1% settling times are set according to Table 9, with no overshoot. The tuning of the PI controller is a well-known topic in literature and can be accomplished with aided-design software as, for example, the *Control System Designer* tool from MATLAB. Therefore, for the sake of brevity, it is not explained in this paper [53]. With the system parameters previously shown in Table 4 and 5, the resulting control parameters are those collected in Table 10. The tracking of the corresponding reference signals for the inner and outer loop controllers is shown in Fig. 11. As expected, the settling time of the inner loop is noticeably lower.

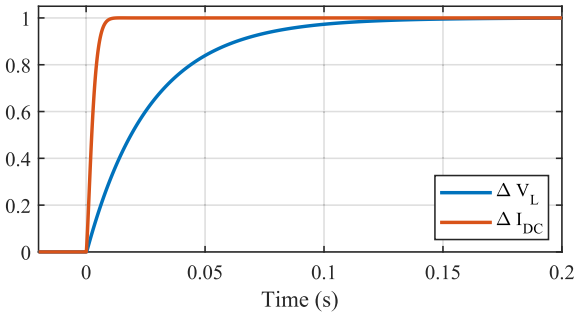

FIGURE 11. Dynamic response of the reference tracking of the inner and outer loop controllers.

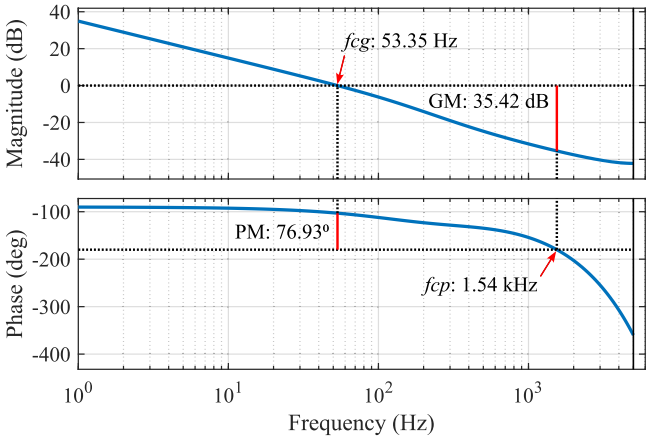

FIGURE 12. Phase and gain margins calculation of the inner control loop.

E. STABILITY ANALYSIS

The calculation of the gain and phase margins in the inner loop is straightforward. Fig. 12 shows the frequency response and the definition of both relative stability margins of the cascaded connection of $R_{In}(z)$, the unit delay, and $H_I(z)$. As a result, a gain margin (GM) of 35.42 dB was obtained at a phase crossover frequency (f_{cp}) of 1.54 kHz, while the phase margin (PM) was 76.93° at a gain crossover frequency (f_{cg}) of 53.35 Hz.

The calculation of the stability margins for the outer control loop requires calculating the equivalent transfer function of the inner loop, H_{eq}:

$$H_{eq}(z) = \frac{z^{-1} R_{In}(z) H_I(z)}{1 + z^{-1} R_{In}(z) H_I(z)} \tag{38}$$

The curve fitting can be represented as a gain in the small signal model. The linearization of the fitting polynomial around the equilibrium point indicated in Fig. 3 yields a linear equation in the form $I_{DC} = a \cdot L_{f1} + b$. The coefficient a multiplying L_{f1} in this equation serves as the gain that represents the curve fitting in the small signal model.

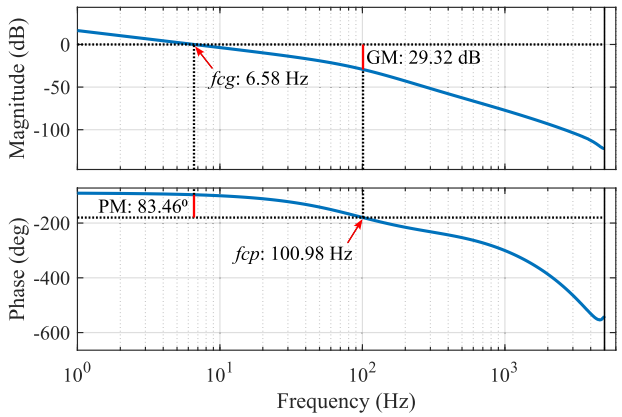

FIGURE 13. Phase and gain margins calculation of the outer control loop.

As stated before, the dynamic behavior of the variable inductor is assumed to be sufficiently fast so that it can be neglected. Consequently, the small signal model of the variable inductor can be regarded as another gain whose calculation is analogous to that of the curve fitting. For this purpose, the axes in Fig. 6 must be interchanged and another curve fitting must be made by following the procedure described previously in Section V-B. Subsequently, the resulting polynomial can be linearized around the equilibrium point. This procedure is exactly the same as the one explained for the curve fitting and therefore it is not further discussed in this article.

After calculating $H_{eq}(z)$ and both gains, the relative stability margins for the outer loop can be obtained. Fig. 13 illustrates the calculation of the stability margins, yielding values of GM $= 29.32$ dB at $f_{cp} = 100.98$ Hz and PM $= 83.46^{\circ}$ at $f_{cg} = 6.58$ Hz.

VI. EXPERIMENTAL RESULTS

A prototype has been designed, assembled, and experimentally tested to validate the proposed control scheme. The experimental set-up is shown in Fig. 14. A GaN Systems GS665EVBMB motherboard with a configuration of a half-bridge inverter and a Siglent SDG1025 waveform generator is used for supplying the voltage waveform at the primary side of the IWPT system. The DC-DC converter driving the auxiliary circuit uses an EPC90122 board that integrates two EPC2206 GaN FET, and the proposed control scheme is programmed in a NUCLEO-H7A3ZI-Q STM32 board. The DC-DC converter current is measured by using an EVCS1803-S-05-00A evaluation board that integrates an MCS1803GS hall-effect sensor, whereas the load voltage is measured by using an AMC3330EVM evaluation board that integrates an AMC3330 isolated operational amplifier. Two Alpha Elettronica AL862S voltage sources were used to generate the DC voltage at the input of the DC-DC converter and the IWPT system. The experimental data was recorded by using a Rohde & Schwartz RTM3004 oscilloscope with an RT-ZC15B hall-effect current probe and a RT-ZHD07 differential voltage probe. The variable inductor proposed in III and represented by Fig. 4 is integrated into the experimental setup. The operating frequency of the DC-DC converter was set to 100 kHz.

Fig. 15 shows an example of the operation of the proposed experimental setup.

Three sets of experiments will be conducted: (i) variations of the coil misalignment, (ii) variations of the loads and (iii) changing the output reference.

Fig. 16 shows the measured load voltages when a DC current of 0 A and 3.75 A are supplied to the coil for different misalignments. These currents correspond to the maximum and minimum inductances reached by L_{f1}, which delimit the operation range shown previously in Fig. 3. The maximum misalignment reached is 150 mm, and the outer diameter of the coils is 250 mm. Therefore, a displacement of up to 60% of the coil size was tested. When comparing 16 and 3, it is obtained that the theoretical values of V_L for the minimum and maximum inductances are very similar to the experimental ones when there is no misalignment. Therefore, a good correlation is obtained between theoretical and experimental values in both operating points.

The shaded area in Fig. 16 indicates all the values for V_L that the system can reach for the different misalignments, that is, the area in which the proposed control scheme can operate without saturating. For example, for a maximum misalignment of 50 mm, a maximum voltage of 35 V can be reached. Therefore, the control scheme will be able to keep this voltage constant until this misalignment is achieved. If V_L^* is kept constant at 35 V for higher misalignments, the control signal will saturate and the obtained values will be those of a 3.75 A. A more illustrative example can be found if V_L^* is set to 25 V. In this situation, the obtained voltage will correspond to the measured values at $I_{DC} = 0$ A until a misalignment of about 70 mm is reached. After this, the desired voltage will be kept constant and, for displacements between coils higher than 90 mm, the obtained values for V_L will be those registered for $I_{DC} = 3.75$ A.

Fig. 17 and Fig. 18 show the system response when two steps from 32 to 40 V and 40 to 32 V are applied in the reference voltage. This change implies a variation of around 20% from the maximum voltage that can be applied to the load. In both cases, a smooth transition of the load voltage is achieved, with no overshoot. The evolution of the measured I_{DC} and V_L as well as the target inductance and the duty cycle applied to the DC-DC converter for both steps is shown in Fig. 19. As the step in V_L^* occurs, the error signal changes suddenly to 8 V. Therefore, the proportional gain of the PI controller varies L_{f1}^* instantaneously by about 1.6 μH, and the inner control loop modifies quickly D to reach the desired I_{DC}^*. After this, the integral part of the PI controller in the outer loop starts modifying L_{f1}^* gradually. As the power transferred to the load is inversely related to L_{f1}, V_L varies accordingly to I_{DC} and, consequently, the smooth transition of V_L is obtained for both steps.

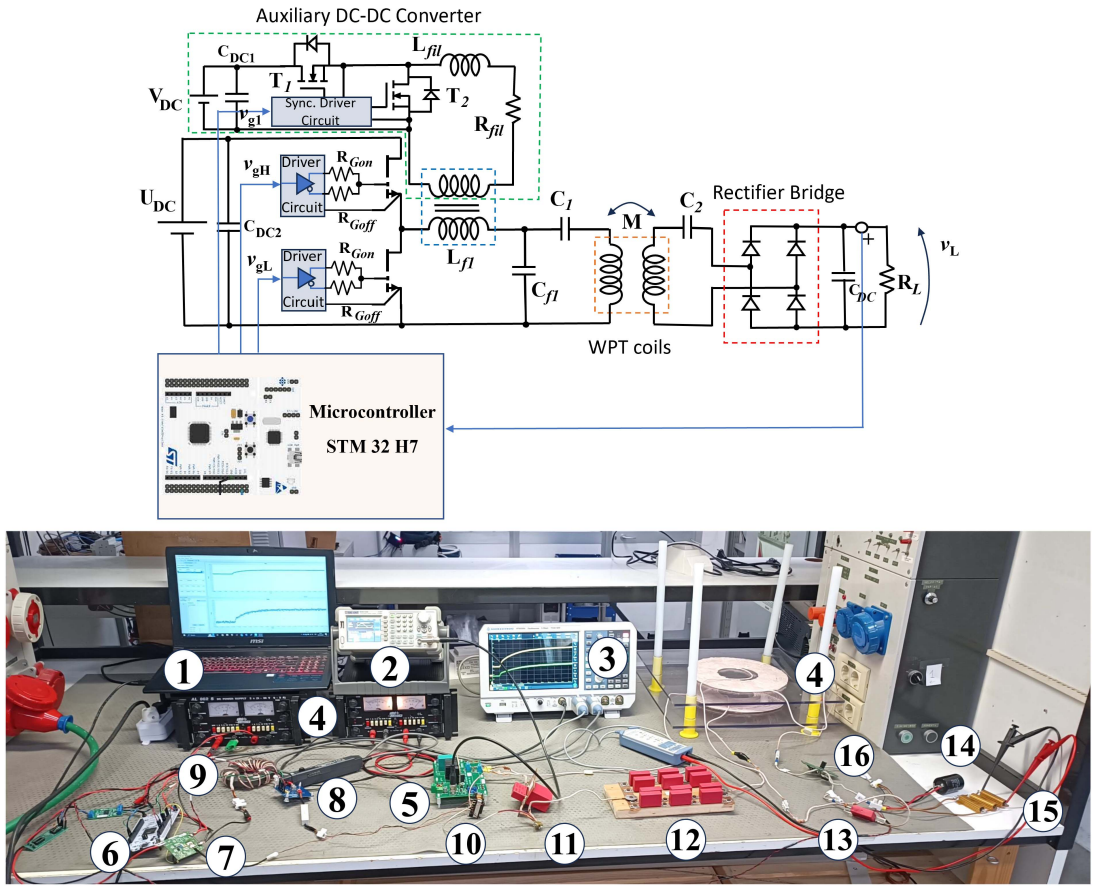

FIGURE 14. (a) Scheme of the experimental set-up. (b) Photo of the experimental set-up: PC (1). Function Generator (2). Oscilloscope (3). Coils (4). Half-Bridge inverter (5). Nucleo-H7A3ZI (6). Hall sensor MCS1803GS (7). Voltage sensor AMC3330EVM (8). L_{fil} (9). L_{f1} (10). C_{f1} (11). C_1 (12). C_2 (13). C_{DC} (14). R_L (15). Rectifier (16).

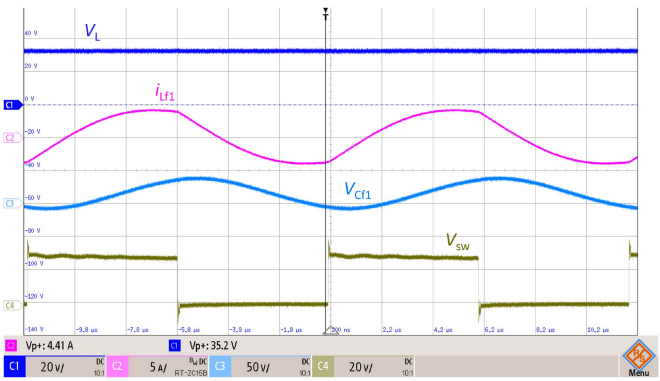

FIGURE 15. Measurements of the load voltage (blue), inductive current on the transmitter side (magenta), voltage on the parallel capacitor C_{f1} (light blue), and voltage of the half-bridge switching node (green).

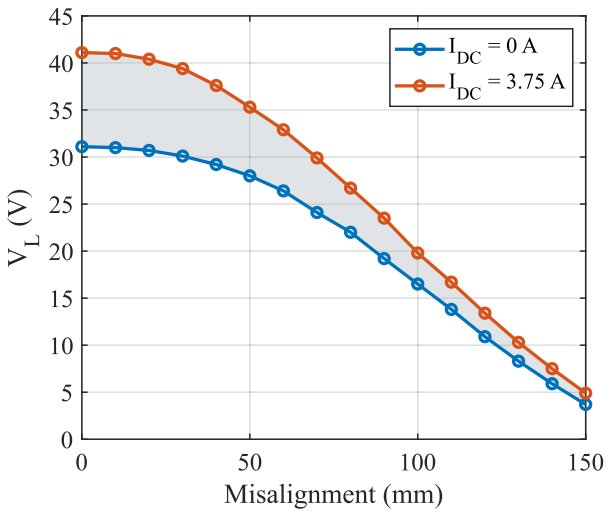

FIGURE 16. Variation of V_L against misalignment.

By comparing the obtained current and voltage waveforms in Fig. 17 and 18, it can be inferred that the trend followed by I_{DC} is very similar to that of V_L. The magnetization in the core increases with the current, and this leads to the core saturation and the respective decrease of the coil inductance. On the other hand, core saturation decreases with the reduction of I_{DC}, increasing its inductance. The similarity of the trends in I_{DC} and V_L reinforces the assumption of an almost-instantaneous change of L_{f1} against I_{DC} variations.

Finally, the disturbance rejection of the proposed control scheme was tested. For this purpose, a step change of 10 Ω

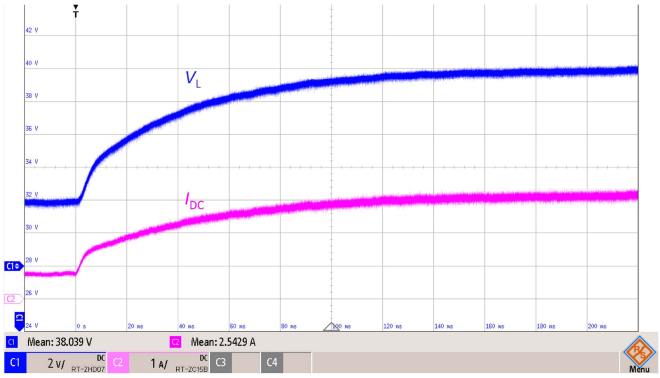

FIGURE 17. Experimental results for a step from 32 to 40V in the load voltage.

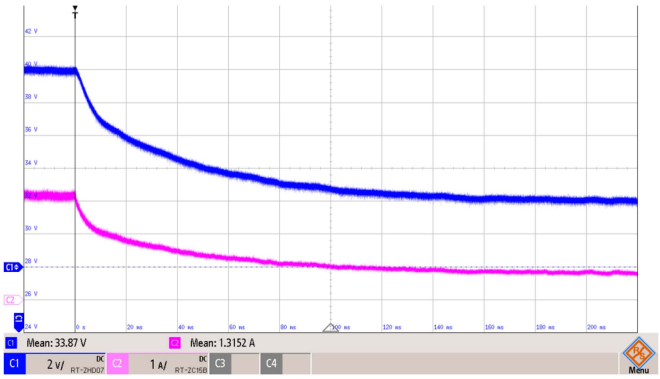

FIGURE 18. Experimental results for a step from 40 to 32V in the load voltage.

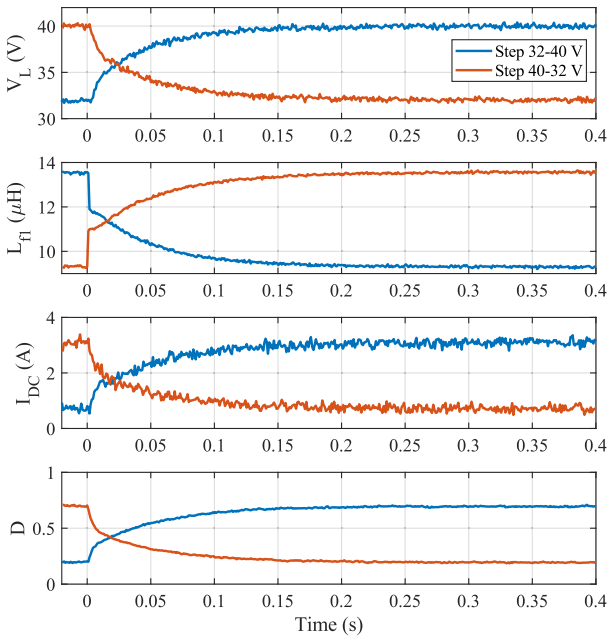

FIGURE 19. Experimental data recorded by the STM32 for the two steps shown in Fig. 17 and 18.

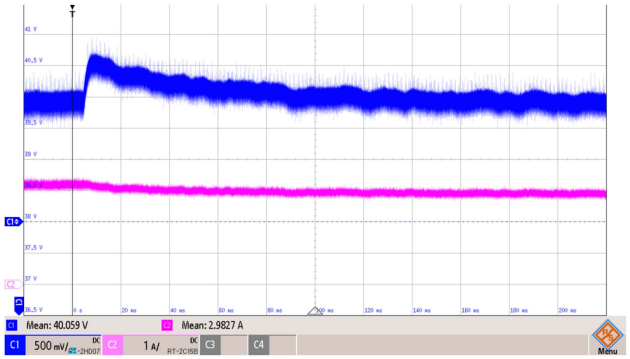

FIGURE 20. Experimental data recorded with the oscilloscope during the disturbance rejection of an increase of 10 Ω in V_L.

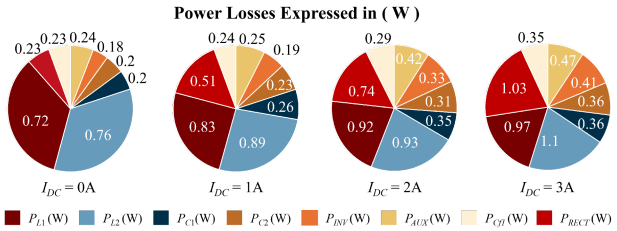

FIGURE 21. Power loss analysis of the WPT system under different operative conditions of the variable inductor.

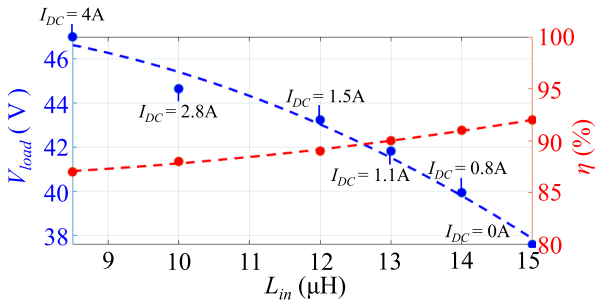

FIGURE 22. Experimental measured output power and efficiency at different operating conditions.

in R_L was applied to the system when $V_L^* = 40$ V, changing the value of R_L from 50 Ω to 60 Ω. The experimental results are shown in Fig. 20. The change on R_L increases V_L and, consequently, the control scheme decreases I_{DC} to obtain a higher L_{f1}, which reduces the current supplied to the load and keeps the voltage at the desired value.

To conclude, the analysis of the power losses of the system is presented in Fig. 21, where the contribution of each conversion element is estimated under different operative conditions of the variable inductor. The power dissipation for capacitors C_{f1}, C_1, and C_2, as well as the transmitter and receiver coils L_1 and L_2, have been reported, along with the losses of the inverter on the transmitter side P_{INV} and the rectifier on the receiver side P_{RECT}. Furthermore, the power losses of the auxiliary circuit P_{AUX} have been measured, taking into account the contributions of the synchronous buck converter and the

variable inductor. Finally, in Fig. 22, the output voltage and the efficiency for different operating conditions are shown. The inductance L_{in} has been modified by regulating the current I_{DC} through the auxiliary circuit.

VII. CONCLUSION

The proposed study introduces an innovative control paradigm tailored for an LCC-S Wireless Power Transfer (WPT) system, wherein the regulation of the system's output voltage relies on a variable inductor exploiting magnetic core saturation. The design methodology for this variable inductor, tailored to specific control requirements, is comprehensively presented. A notable contribution of this work is the development of a small signal model, addressing a substantial gap in current literature by establishing a clear correlation between output voltage variations and changes in inductance. The proposed approach pioneers a transfer function, offering a precise portrayal of this dynamic behavior.

Furthermore, the paper proposes a closed-loop control system designed to swiftly adjust the output voltage, showcasing effectiveness in managing rapid load variations and misalignment challenges, thus ensuring robust regulation. The efficacy of the proposed approach is substantiated through extensive experimental measurements, validating theoretical and simulation outcomes.

Noteworthy analyses of the system's performance under three distinct conditions were conducted. Firstly, under variations in the output reference, secondly, in the presence of load variations, and thirdly, during coil misalignment. The study analyzes the operational envelope extension attributable to the proposed control technique, providing valuable insights into its adaptability and reliability across a spectrum of operational scenarios.

REFERENCES

[1] V. -B. Vu et al., "Operation of inductive charging systems under misalignment conditions: A review for electric vehicles," *IEEE Trans. Transp. Electrific.*, vol. 9, no. 1, pp. 1857–1887, Mar. 2023, doi: 10.1109/TTE.2022.3165465.

[2] J.-Y. Lee and B.-M. Han, "A bidirectional wireless power transfer EV charger using self-resonant PWM," *IEEE Trans. Power Electron.*, vol. 30, no. 4, pp. 1784–1787, Apr. 2015.

[3] C. Xia et al., "Simultaneous wireless power and multibit signals transfer system with hybrid modulation waves PWM control," *IEEE Trans. Power Electron.*, vol. 37, no. 10, pp. 12913–12928, Oct. 2022, doi: 10.1109/TPEL.2022.3178998.

[4] P. M. -Y. Fan and M. H. bin Mohd Daut, "Near-unity power factor, voltage step-up/down conversion pulse-width modulated switching rectification for wireless power transfer receiver," *IEEE Trans. Power Electron.*, vol. 34, no. 11, pp. 10960–10969, Nov. 2019.

[5] C. Zhao and D. Costinett, "GaN-Based dual-mode wireless power transfer using multifrequency programmed pulse width modulation," *IEEE Trans. Ind. Electron.*, vol. 64, no. 11, pp. 9165–9176, Nov. 2017, doi: 10.1109/TIE.2017.2681974.

[6] I. -W. Iam et al., "Constant-frequency and noncommunication-based inductive power transfer converter for battery charging," *IEEE Trans. Emerg. Sel. Topics Power Electron.*, vol. 10, no. 2, pp. 2147–2162, Apr. 2022, doi: 10.1109/JESTPE.2020.3004259.

[7] Y. Zhou, Z. Zhang, P. Dong, Y. Chen, and L. Huang, "Simultaneous wireless power and data transmission based on unsymmetrical current waveforms with duty cycle modulation," *IEEE Access*, vol. 8, pp. 16495–16504, 2020, doi: 10.1109/ACCESS.2020.2966664.

[8] K. Li, S.-C. Tan, and S. Y. R. Hui, "Efficient hybrid-modulated single-stage wireless power receiver with continuous DC current," *IEEE Trans. Power Electron.*, vol. 36, no. 12, pp. 13504–13514, Dec. 2021, doi: 10.1109/TPEL.2021.3072101.

[9] S.-T. Wu and C.-H. Han, "Design and implementation of a full-bridge LLC converter with wireless power transfer for dual mode output load," *IEEE Access*, vol. 9, pp. 120392–120406, 2021.

[10] G. Namgoong, H. Park, and F. Bien, "A real-time calibrated Adaptive-ZVS class-D power amplifier for 6.78 MHz wireless power transfer system," *IEEE Trans. Circuits Syst. II, Exp. Briefs*, vol. 69, no. 9, pp. 3794–3798, Sep. 2022.

[11] Z. Hua, K. T. Chau, W. Liu, and X. Tian, "Pulse frequency modulation for parity-time-symmetric wireless power transfer system," *IEEE Trans. Magn.*, vol. 58, no. 8, Aug. 2022, Art. no. 8002005, doi: 10.1109/TMAG.2022.3153499.

[12] Z. Hua, K. T. Chau, W. Liu, X. Tian, and H. Pang, "Autonomous pulse frequency modulation for wireless battery charging with zero-voltage switching," *IEEE Trans. Ind. Electron.*, vol. 70, no. 9, pp. 8959–8969, Sep. 2023, doi: 10.1109/TIE.2022.3215814.

[13] W. Liu, K. T. Chau, C. H. T. Lee, W. Han, X. Tian, and W. H. Lam, "Full-range soft-switching pulse frequency modulated wireless power transfer," *IEEE Trans. Power Electron.*, vol. 35, no. 6, pp. 6533–6547, Jun. 2020, doi: 10.1109/TPEL.2019.2952573.

[14] W. Han, K. T. Chau, L. Cao, Z. Hua, and T. Yang, "S-CLC compensated wireless power transfer with pulse-frequency-modulation control for dimmable low-pressure sodium lamps," *IEEE Trans. Magn.*, vol. 57, no. 2, Feb. 2021, Art. no. 8001107.

[15] Y. Zhang, S. Chen, X. Li, and Y. Tang, "Dual-side phase-shift control of wireless power transfer implemented on primary side based on driving windings," *IEEE Trans. Ind. Electron.*, vol. 68, no. 9, pp. 8999–9002, Sep. 2021, doi: 10.1109/TIE.2020.3013522.

[16] E. Ayaz, O. Altun, and O. Keysan, "Carrier phase shift method of SPWM for concurrent wired and wireless power transfer systems," *IEEE Trans. Ind. Electron.*, vol. 70, no. 9, pp. 8645–8654, Sep. 2023, doi: 10.1109/TIE.2022.3213908.

[17] Q. W. Low, M. Zhou, and L. Siek, "A single-stage direct-conversion AC–DC converter for inductively powered application," *IEEE Trans. Very Large Scale Integration Syst.*, vol. 26, no. 5, pp. 892–902, May 2018, doi: 10.1109/TVLSI.2018.2792494.

[18] J. Tang, T. Na, and Q. Zhang, "A novel full-bridge step density modulation for wireless power transfer systems," *IEEE Trans. Power Electron.*, vol. 38, no. 1, pp. 41–45, Jan. 2023.

[19] R. Dai, W. Zhou, Y. Chen, Z. Zhu, and R. Mai, "Pulse density modulation based mutual inductance and load resistance identification method for wireless power transfer system," *IEEE Trans. Power Electron.*, vol. 37, no. 8, pp. 9933–9943, Aug. 2022.

[20] R. Dai, R. Mai, and W. Zhou, "A pulse density modulation based receiver reactance identification method for wireless power transfer system," *IEEE Trans. Power Electron.*, vol. 37, no. 9, pp. 11394–11405, Sep. 2022, doi: 10.1109/TPEL.2022.3167265.

[21] H. Li, K. Wang, J. Fang, and Y. Tang, "Pulse density modulated ZVS full-bridge converters for wireless power transfer systems," *IEEE Trans. Power Electron.*, vol. 34, no. 1, pp. 369–377, Jan. 2019.

[22] F. Grazian, T. B. Soeiro, and P. Bauer, "Inductive power transfer based on variable compensation capacitance to achieve an EV charging profile with constant optimum load," *IEEE Trans. Emerg. Sel. Topics Power Electron.*, vol. 11, no. 1, pp. 1230–1244, Feb. 2023, doi: 10.1109/JESTPE.2022.3188060.

[23] J. Zhang, J. Zhao, L. Mao, J. Zhao, Z. Jiang, and K. Qu, "ZVS operation of class-E inverter based on secondary side zero compensation switching at variable coupling coefficient in WPT," *IEEE Trans. Ind. Appl.*, vol. 58, no. 1, pp. 1022–1031, Jan.–Feb. 2022.

[24] R. Matsumoto, T. Fujita, and H. Fujimoto, "Communicationless reactance compensation using PWM-Controlled switched capacitors for wireless power transfer," *IEEE Trans. Power Electron.*, vol. 38, no. 10, pp. 13194–13206, Oct. 2023.

[25] J. Zhang, J. Zhao, Y. Zhang, and F. Deng, "A wireless power transfer system with dual switch-controlled capacitors for efficiency optimization," *IEEE Trans. Power Electron.*, vol. 35, no. 6, pp. 6091–6101, Jun. 2020, doi: 10.1109/TPEL.2019.2950218.

[26] W. Li, G. Wei, C. Cui, X. Zhang, and Q. Zhang, "A double-side self-tuning LCC/S system using a variable switched capacitor based on parameter recognition," *IEEE Trans. Ind. Electron.*, vol. 68, no. 4, pp. 3069–3078, Apr. 2021.

[27] J. Li, J. Wang, J. Li, and J. Chen, "Multivariable coordinated control strategy for efficiency optimization without real-time wireless feedback communication in wireless power transfer," *IEEE Access*, vol. 10, pp. 55381–55395, 2022.
[28] Y. Hou et al., "Wireless power transfer system based on LCC/LCL-S variable structure with constant output power," *Energy Rep.*, vol. 8, pp. 850–862, 2022.
[29] Y. Lim, H. Tang, S. Lim, and J. Park, "An adaptive impedance-matching network based on a novel capacitor matrix for wireless power transfer," *IEEE Trans. Power Electron.*, vol. 29, no. 8, pp. 4403–4413, Aug. 2014, doi: 10.1109/TPEL.2013.2292596.
[30] V. Bertolini, F. Corti, M. Intravaia, A. Reatti, and E. Cardelli, "Optimizing power transfer in selective wireless charging systems: A genetic algorithm-based approach," *J. Magnetism Magn. Mater.*, vol. 587, Dec. 2023, Art. no. 171340. [Online]. Available: https://doi.org/10.1016/j.jmmm.2023.171340
[31] D. Thenathayalan and J.-H. Park, "Highly flexible high-efficiency multiple-resonant wireless power transfer system using a controllable inductor," *IEEE Trans. Emerg. Sel. Topics Power Electron.*, vol. 7, no. 3, pp. 1914–1930, Sep. 2019.
[32] S. Aldhaher, P. C.-K. Luk, and J. F. Whidborne, "Electronic tuning of misaligned coils in wireless power transfer systems," *IEEE Trans. Power Electron.*, vol. 29, no. 11, pp. 5975–5982, Nov. 2014, doi: 10.1109/TPEL.2014.2297993.
[33] H. Zhang, Y. Chen, D.-H. Kim, Z. Li, M. Zhang, and G. Li, "Variable inductor control for misalignment tolerance and constant current/voltage charging in inductive power transfer system," *IEEE Trans. Emerg. Sel. Topics Power Electron.*, vol. 11, no. 4, pp. 4563–4573, Aug. 2023, doi: 10.1109/JESTPE.2023.3281891.
[34] Z. Li, H. Liu, Y. Huo, J. He, Y. Tian, and J. Liu, "High-misalignment tolerance wireless charging system for constant power output using dual transmission channels with magnetic flux controlled inductors," *IEEE Trans. Power Electron.*, vol. 37, no. 11, pp. 13930–13945, Nov. 2022, doi: 10.1109/TPEL.2022.3181231.
[35] J. Li, C. Zhu, J. Xie, F. Lu, and X. Zhang, "Design and implementation of high-misalignment tolerance WPT system for underwater vehicles based on a variable inductor," *IEEE Trans. Power Electron.*, vol. 38, no. 10, pp. 11726–11737, Oct. 2023.
[36] L. Solimene, F. Corti, S. Musumeci, A. Reatti, and C. S. Ragusa, "A controlled variable inductor for an LCC-S compensated wireless power transfer system," in *IECON 2022 IEEE 48th Annu. Conf. Ind. Electron. Soc.*, Oct. 2022, pp. 1–6. doi: 10.1109/IECON49645.2022.9968576.
[37] L. Solimene, F. Corti, S. Musumeci, C. S. Ragusa, and A. Reatti, "Magnetic control of LCC-S compensated wireless power transfer system," in *2022 IEEE Int. Symp. Power Electron. Elect. Drives Automat. Motion*, Sorrento, Italy, Jun. 2022, pp. 160–165. doi: 10.1109/SPEEDAM53979.2022.9842241.
[38] Y. Wei, D. Woldegiorgis, and A. Mantooth, "Variable resonant and magnetizing inductor control for LLC resonant converter," in *2020 IEEE 11th Int. Symp. Power Electron. Distrib. Gener. Syst.*, Dubrovnik, Croatia, 2020, pp. 149–153.
[39] Y. Wei, Q. Luo, and A. Mantooth, "Comprehensive analysis and design of LLC resonant converter with magnetic control," *CPSS Trans. Power Electron. Appl.*, vol. 4, no. 4, pp. 265–275, Dec. 2019, doi: 10.24295/CPSSTPEA.2019.00025.
[40] A. P. Mendes, B. Baptista, M. S. Perdigão, and A. M. S. Mendes, "Experimental analysis of a DC current-controlled variable inductor in a DC–DC converter," in *2019 IEEE Int. Conf. Ind. Technol.*, Melbourne, VIC, Australia, 2019, pp. 440–445.
[41] S. M. Ahsanuzzaman, T. McRae, M. M. Peretz, and A. Prodić, "Low-volume buck converter with adaptive inductor core biasing," in *2012 IEEE 27th Annu. Appl. Power Electron. Conf. Expo.*, Orlando, FL, USA, 2012, pp. 335–339.
[42] K. Bao-quan, T. Hong-jiang, and L. Ying-qi, "Research of adjustable inverter output filter based on DC magnetic flux controllable inductor," in *2008 IEEE Veh. Power Propulsion Conf.*, Harbin, China, 2008, pp. 1–5, doi: 10.1109/VPPC.2008.4677672.
[43] H. Chinchero and M. Alonso, "Using magnetic control of DC-DC converters in LED driver applications," *IEEE Latin Amer. Trans.*, vol. 19, no. 2, pp. 297–305, Feb. 2021.
[44] S. Saeed and J. Garcia, "Extended operational range of dual-active-bridge converters by using variable magnetic devices," in *2019 IEEE Appl. Power Electron. Conf. Expo.*, Anaheim, CA, USA, 2019, pp. 1629–1634, doi: 10.1109/APEC.2019.8721920.
[45] L. Solimene, F. Corti, S. Musumeci, C. S. Ragusa, A. Reatti, and E. Cardelli, "Design and modelling of a controlled saturable inductor for an LCC-S compensated WPT system," *J. Magnetism Magn. Mater.*, vol. 564, Part 2, Dec. 2022. [Online]. Available: https://doi.org/10.1016/j.jmmm.2022.170056
[46] L. Solimene, F. Corti, S. Musumeci, F. J. López-Alcolea, A. Reatti, and C. S. Ragusa, "Experimental validation of magnetic control strategy in LCC-S compensated wireless power transfer systems," *IET Power Electron.*, vol. 17, no. 8, pp. 919–929, 2024, doi: 10.1049/pel2.12718.
[47] N. Mohan, Tore M. Undeland, and William P. Robbins, *Power Electronics: Converters, Applications, and Design*. Hoboken, NJ, USA: Wiley, 2003.
[48] Y. Chen, H. Zhang, S. -J. Park, and D. -H. Kim, "A switching hybrid LCC-S compensation topology for constant current/voltage EV wireless charging," *IEEE Access*, vol. 7, pp. 133924–133935, 2019.
[49] L. Solimene, D. Cittanti, F. Mandrile, S. Musumeci, and R. Bojoi, "Optimal air gap length design in powder core inductors," *IEEE Trans. Magn.*, vol. 59, no. 11, Nov. 2023, Art. no. 8401505, doi: 10.1109/TMAG.2023.3289391.
[50] J. Muhlethaler, J. Biela, J. W. Kolar, and A. Ecklebe, "Core losses under the DC bias condition based on steinmetz parameters," *IEEE Trans. Power Electron.*, vol. 27, no. 2, pp. 953–963, Feb. 2012, doi: 10.1109/TPEL.2011.2160971.
[51] H. Li, D. Serrano, S. Wang, and M. Chen, "MagNet-AI: Neural network as datasheet for magnetics modeling and material recommendation," *IEEE Trans. Power Electron.*, vol. 38, no. 12, pp. 15854–15869, Dec. 2023, doi: 10.1109/TPEL.2023.3309233.
[52] "MagNet." Accessed: Feb. 9, 2024. [Online]. Available: https://magnet.princeton.edu/
[53] L. Wang, *PID Control System Design and Automatic Tuning Using MATLAB/Simulink*. Hoboken, NJ, USA: Wiley, 2020.

Open Access provided by 'Università degli Studi di Firenze' within the CRUI CARE Agreement